

# Limitations on estimation of effective scatterer diameters

Yang Zhu,<sup>1,a),b)</sup> Aiguo Han,<sup>2,b)</sup> William D. O'Brien, Jr.,<sup>2,b)</sup> Michael L. Oelze,<sup>2,b)</sup>  
 and Michael F. Insana<sup>1,b)</sup>

<sup>1</sup>Department of Bioengineering, University of Illinois at Urbana-Champaign, 1304 West Springfield Avenue, Urbana, Illinois 61801, USA

<sup>2</sup>Department of Electrical and Computer Engineering, University of Illinois at Urbana-Champaign, 306 North Wright Street, Urbana, Illinois 61801, USA

(Received 9 May 2017; revised 17 November 2017; accepted 23 November 2017; published online 19 December 2017)

The influence of spatial diversity in acoustic scattering properties on estimates of the effective scatterer diameter (ESD) applied to soft biological tissues is investigated. This study is based on two-dimensional simulations of scattering media, beginning with random distributions of simple disk structures where all scattering features are known exactly. It concludes with an analysis of histology maps from healthy and fatty rabbit liver. Further, the liver histology is decomposed using an orthonormal basis to separate acoustic scattering at various spatial scales and observe how it influences ESD estimates. Overall, the goal is to quantitatively interpret ESD results for diagnostic assessments despite wide variations in tissue scatterer properties. © 2017 Acoustical Society of America.

<https://doi.org/10.1121/1.5017602>

[CCC]

Pages: 3677–3690

## I. INTRODUCTION

Ever since the basic sources of acoustic scattering in soft tissues were first identified,<sup>1</sup> many investigators have worked to discover how ultrasonic scattering features might serve as sensitive biomarkers of early disease.<sup>2–11</sup> The long history of safe use, relatively low cost, and the phase-sensitive nature of detection make ultrasonic methods well suited for the task of noninvasive histological assessment. However, the relationship between echo spectra and the tissue structure from which they arise is complicated by histological variability.

Pathology is defined by the changes in cellular function and histology caused by a disease process. Parametric models of pulse-echo ultrasound offer *in vivo* alternatives to light microscopy of fixed biopsy samples when the parameters describe spatially averaged features of *in situ* cellular architecture. The elements of parenchymal tissues that interact with sound waves at diagnostic imaging frequencies are close-packed polydisperse cells and associated structures. Incident wave energy is partially reflected at any spatial fluctuation in mass density and bulk compressibility.<sup>12</sup> The spectrum of reflecting structures at the 5–45  $\mu\text{m}$  size scale includes microvascular networks, individual cells, and cell nuclei.<sup>1,6</sup>

Because mass density and compressibility are relatively uniform within soft parenchymal tissues, acoustic scattering from parenchymal tissues is weak, i.e., backscatter coefficients<sup>2,13</sup> range between  $10^{-6}$  and  $10^{-3} \text{ cm}^{-1} \text{ sr}^{-1}$ . Consequently, echographic contrast is primarily determined by regional variations in the concentrations and sizes of cell-based structures relative to the wavelength of sound,  $\lambda_0$ , near the pulse transmission frequency  $f_0 = c/\lambda_0$  at the

compressional sound speed  $c$ . For symmetric scatterers of radius  $a$ , the sensitivity of the echo signal to that reflector is indicated by the ratio of scatterer circumference to wavelength,  $2\pi a/\lambda_0 = ka$ , where  $k$  is the wave number. Scatterer size can be measured with minimal prior information regarding reflector shape and orientation using spectral methods<sup>4,8,10,14–16</sup> when the propagation medium is composed of randomly positioned monodisperse structures at pulse-echo frequencies near  $ka = 1$ ,<sup>7,17</sup> e.g., unclotted red blood cells<sup>18</sup> near 60 MHz. However, soft tissues are composed of polydisperse structures. Thus, when interrogated by broadband pulses, echo signals from tissues comprise a broad range of  $ka$  values each with a different contribution to the measured echo. Unequal weighting means the average scatterer size measured from tissue echo spectra is not the average size seen histologically.

This report uses echo simulations to investigate the accuracy of a biased metric that has shown diagnostic utility,<sup>16,19–21</sup> the effective scatterer diameter (ESD).<sup>8,10</sup> In the long-wavelength limit, where  $ka \ll 1$ , the echoes are weakest as reflectors interact with sound as point targets. We will show that ESD measurement bias at  $ka \ll 1$  stems primarily from noise in the echo spectrum. Conversely, more reflective tissue structures that contribute in the short-wavelength limit, at  $ka \gg 1$ , require significant prior knowledge about fine-scale histological properties to avoid ESD bias. Despite measurement bias and the effects of polydisperse scatterers, we will show that ESD measurements can be effectively interpreted for histological changes in space and time.

We first summarize ESD measurement techniques from pulse-echo backscattered spectra. The standard approach assumes tissues are a weakly-interacting isotropic random media. Echo signals recorded for spectral analysis are modeled as wide-sense stationary processes convolved with shift-invariant acoustic pulses in white Gaussian acquisition noise. Spatially averaged echo power-spectral density estimates are

<sup>a)</sup>Electronic mail: yangzhu2@illinois.edu

<sup>b)</sup>Also at Beckman Institute for Advanced Science and Technology, University of Illinois at Urbana-Champaign, 405 N. Mathews Ave, Urbana IL 61801, USA.

influenced by properties of the pulse, the spatial distribution of tissue reflector sizes, and noise. The ESD measurement process describes tissue structure by fitting a measured echo spectrum for a region to a model spectrum parameterized by a characteristic size.<sup>9</sup> Reflectivity and concentration of tissue scatterers modify the overall magnitude of the echo spectrum. However, a weighted sum of scattering functions defined by the spatial autocorrelation of tissue impedance fluctuations having sizes near  $ka \simeq 1$  determines the spectral shape.<sup>4,7</sup> The general approach is to model histology by its spatial autocorrelation function to infer the average size of structure contributing to the echo spectrum. This method has been widely applied to measurements in monodisperse<sup>10,14,16,22–24</sup> and polydisperse biological media.<sup>15,17,25</sup>

Our study is an exploration of ESD measurements from simulated two-dimensional (2-D) scattering media and sound pulses. Initially, the scattering fields are weakly-reflecting, cell-sized disks with known sizes and random positional distributions. Later, we replace the random disk fields with rabbit-liver histology to introduce 2-D tissue-like structural complexity to the scattering field. To evaluate contributions from diverse and dense histological structures at various size scales, we first filtered a basis decomposition of liver histology images before simulating echo signals. We then applied structure-function filtering to the simulated echo signal to minimize coherent scattering effects.<sup>26</sup> These two filters allow us to uncouple and isolate cellular components based on reflector size to measure the contribution of each to ESD measurements.

Echo-signal simulations were analyzed using a 2-D scattering theory to make the task computationally realistic. We first approached a three-dimensional (3-D) simulator using a 2-mm cubic volume of tissue. Each histology image was sampled at  $0.46 \mu\text{m}$  in two in-plane dimensions of the histology image and  $3 \mu\text{m}$  in thickness, generating a data array with  $1.3 \times 10^{10}$  elements. 3-D convolutions were manageable because the 2-D outputs were downsampled by a factor of 42 along the beam axis and 220 laterally to match common commercial-system sampling intervals of 0.019 mm axially (40 Msamples/s sampling rate) and 0.1 mm laterally (pitch of a linear array). However, direct full-field 3-D basis decompositions required diagonalization of matrices of size  $10^{20} \times 10^{20}$ , well beyond memory capacity. Piecewise 3-D decompositions required more than 24 h on a multi-core laptop. In contrast, 2-D in-plane histological decompositions

were computed in less than two hours, realistically enabling the analysis of hundreds of data sets for this study.

Our results suggest that polydisperse tissues interrogated by broadband pulses generate echo-signal spatial covariance matrices of low rank with respect to ESD measurements. Consequently, measurement bias does not adversely affect spatial variations in ESD. While bias affects absolute measurements, ESD bias does not modify relative measurements that determine scatterer-size image contrast.

## II. METHODS

### A. Backscatter coefficient model

A general expression for the *modeled* backscatter coefficient is<sup>8,12</sup>

$$\sigma_b(k) = \bar{n} |\Phi(2k)|^2, \quad (1)$$

which assumes an incident plane wave of unit intensity and wave number  $k = 2\pi/\lambda$ . The squared magnitude of the scattering amplitude,

$$|\Phi(2k)|^2 = \frac{k^3}{4\pi^2} \left| \int_A d\mathbf{r}' \gamma(\mathbf{r}') e^{-i\mathbf{K}\cdot\mathbf{r}'} \right|^2, \quad (2)$$

approximates a 2-D scattering field by assuming a random spatial distribution of scattering cylinders with axes aligned perpendicular to the incident field.<sup>12</sup>  $\gamma(\mathbf{r}')$  describes the variation in acoustic impedance relative to the surroundings as disk-shaped cross sections of the cylinders (Fig. 1). Disks are located at vector position  $\mathbf{r}'$  relative to a reference point on the receive aperture of a transducer.  $\mathbf{K}$  is a scattering vector describing the momentum transfer; its magnitude is  $|\mathbf{K}| = 2k$  for backscatter.  $\bar{n}$  is the number of scatterers per measurement area  $A$ , which for weakly scattering random media yields a completely incoherent scattering field. That is, the net backscattered power is a linear summation of backscattered powers from each scatterer in  $A$ .

We can take advantage of the polar symmetry for plane waves normally incident on discrete cylinders of radius  $a$  by combining Eqs. (1) and (2) to give the 1-D integral equation parameterized by  $a$ ,

$$\sigma_b(k; a) = \bar{n} k^3 \left| \int_{r=0}^{\infty} dr r \gamma(r; a) J_0(2kr) \right|^2, \quad (3)$$

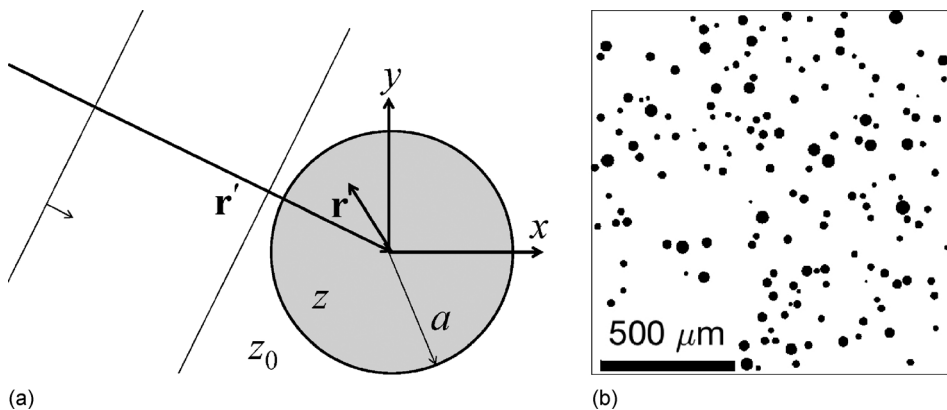


FIG. 1. 2-D impedance maps simulating random placements of discrete fluid-disk scatterers to validate the acoustic measurements. (a) In a fluid disk of radius  $a$ , the impedance inside and outside the disk are  $z$  and  $z_0$ , respectively. Incident plane waves at location  $\mathbf{r}'$  from the detector are scattered depending on properties at position  $\mathbf{r}' + \mathbf{r}$ . (b) Simulated impedance field where fluid-disk diameters are normally distributed with mean  $\mu = 30 \mu\text{m}$  and standard deviation  $\sigma = 9 \mu\text{m}$ .

where  $J_0(\cdot)$  is a zeroth-order Bessel function. Below, we introduce disk functions for  $\gamma(r; a)$  in Eq. (3) to simulate backscatter coefficients for random 2-D media characterized by scatterers having characteristic size  $a$ . We measure ESD by comparing Eq. (3) with measured backscatter coefficients (MBSCs) that are computed from Monte Carlo simulations now described.

## B. Monte Carlo echo simulation

For echo simulations, 2-D object scattering field parameterized by size  $a$  is denoted  $f'(x, y; a)$  or simply  $f'(x, y)$ .  $f'$  is a specific field composed of randomly positioned  $\gamma$  functions. Echo signals  $g(x, y)$  are recorded from objects assuming a linear shift-invariant (LSI) measurement system given by the 2-D convolution  $g(x, y) = [h * * f'](x, y)$ .<sup>27</sup> The LSI pulse-echo impulse response is a Gaussian-modulated sinusoid,

$$h(x, y) = \exp\left[-\frac{1}{2}\left(\left(\frac{x}{\sigma_x}\right)^2 + \left(\frac{y}{\sigma_y}\right)^2\right)\right] \sin(k_0 x), \quad (4)$$

where  $\sigma_x, \sigma_y$  are pulse-width parameters of the Gaussian envelope along the axial and lateral axes, respectively. For temporal transmission frequency  $f_0$ , the corresponding radial spatial frequency is  $k_0 = 4\pi f_0/c$ . ‘‘Axial’’ and ‘‘lateral’’ refer to directions along and perpendicular to pulse propagation, respectively. We set  $\sigma_x$  (mm) =  $0.5/(f_0$  (MHz)). For example, a 10 MHz pulse profile has  $\sigma_x = 0.05$  mm (58% axial bandwidth<sup>28</sup>). We also set  $\sigma_y = 2.5\sigma_x = 0.125$  mm.

Pulse profile  $h$  and object scattering function  $f'$  are each sampled uniformly on the symmetric interval  $\Delta x = \Delta y = 0.00046$  mm. Consequently, the spatial axes are  $x = p\Delta x$  and  $y = q\Delta y$  for integers  $1 \leq p \leq P$  and  $1 \leq q \leq Q$ , where  $P \times Q$  is the size of  $f'[p, q]$ , a symmetrically sampled copy of  $f'(x, y)$ .

Simulated echo data are sampled more coarsely than the object and pulse functions. We always sample echo signals along the lateral axis on the interval  $\Delta y' = 0.1$  mm. This is a common pitch for linear-array transducers in this frequency range that often determines the distance between adjacent axial lines of sight in images. Axial sampling was varied depending on  $f_0$ . For pulse frequencies between 7 and 18 MHz, echoes were sampled on the interval  $\Delta x' = 0.02$  mm corresponding to a 38.5 Msamples/s temporal rate. For pulses in the range 18–27 MHz,  $\Delta x' = 0.01$  mm corresponding to a 77 Msamples/s temporal rate. At 27–45 MHz,  $\Delta x' = 0.0067$  mm corresponding to a 115 Msamples/s temporal rate. Variable rates were applied to minimize both aliasing and computations for each pulse frequency range.

The echo field  $g(x', y')$  was computed for integers  $p', q'$  at discrete locations  $x' = p'\Delta x', y' = q'\Delta y'$  using the 2-D convolutional sum,

$$g[p', q'] = \sum_{p=1}^P \sum_{q=1}^Q h[p' - p, q' - q] f'[p, q; a],$$

where  $1 \leq p' \leq P'$  and  $1 \leq q' \leq Q'$ . (5)

No acquisition noise was introduced.

## C. Estimation of MBSC and ESD

The MBSC is computed from the ratio of two power spectral density functions. First, we find one-dimensional (1-D) axial power spectral density in a region of interest and average the results laterally. Specifically, for forward short-time Fourier-transform operator  $\mathcal{F}$ , we have from Eq. (5)  $(1/P'Q') \sum_{q'=1}^{Q'} |\mathcal{F}_{x'}\{g[p', q']\}|^2$ . Second, we find the axial power spectral density along  $q'_c$ , the center line of the deterministic sound pulse,  $(1/P') |\mathcal{F}_{x'}\{h[p', q'_c]\}|^2$ . The ratio yielding the measurement is

$$\text{MBSC}(k) = \frac{1}{Q'} \frac{\sum_{q'=1}^{Q'} |\mathcal{F}_{x'}\{g[p', q']\}|^2}{|\mathcal{F}_{x'}\{h[p', q'_c]\}|^2}$$

for  $k_{\min} \leq k \leq k_{\max}$ . (6)

The denominator minimizes the influence of the pulse spectrum on the shape of the echo spectrum in the numerator. In this way, MBSC is comparable to the linear model  $\sigma_b$  in Eq. (3) that assumed incident plane waves at frequencies in the discrete measurement bandwidth,  $k_{\min} \leq k \leq k_{\max}$ . Clinical systems with shift-varying impulse responses can be normalized using a reference-phantom technique for implementing ESD measurements.<sup>29</sup>

ESD is estimated<sup>25</sup> from parameter  $a$ , which minimizes the following objective function over the measurement bandwidth,

$$\text{ESD} = 2a \text{ for } \arg \min_a \sum_{k=k_{\min}}^{k_{\max}} [\psi(k, a) - \psi_0(a)]^2, \quad (7)$$

where

$$\psi(k, a) = \log\left(\frac{\text{MBSC}(k)}{S(k) \times \sigma_b(k; a)}\right) \text{ and}$$

$$\psi_0(a) = \frac{1}{K} \sum_{k=k_{\min}}^{k_{\max}} \psi(k, a). \quad (8)$$

MBSC in Eq. (6) does not include all frequency-independent scaling factors that makes it directly comparably to  $\sigma_b$  in Eq. (3). Nevertheless, subtracting  $\psi_0(a)$  within the minimization of Eq. (7) yields accurate ESD estimates for weakly scattering media. The measurement bandwidth given by  $0.8f_0$  was found reliable because of the lack of acquisition noise in the simulations. For example, the fit range in Eqs. (7) and (8) for a 10 MHz pulse with 58% pulse bandwidth is 6–14 MHz ( $k_{\min} = 7.8 \text{ mm}^{-1}$  and  $k_{\max} = 18.2 \text{ mm}^{-1}$ ).

The backscatter coefficient model of Eq. (3) assumes incoherent scattering from sparse random media. As scatterer density increases, a nonrandom phase relationship develops among scattering sites that adds a coherent scattering component to the echo signal. Coherent scattering modifies the shape of the echo spectrum in ways not accounted for by the model. To avoid ESD bias, we corrected MBSC estimates in Eq. (8) for phase correlations in  $f'$  using *structure function*  $S(k)$ .

The structure function was developed by Han and O'Brien<sup>26,30</sup> from the original work of Twersky.<sup>24</sup>  $S(k)$  minimizes coherent scattering by reshaping the echo spectrum to reduce phase correlations. (See Appendix B.) Our simulations provided values of  $r'_j$  for the  $j$ th scatterer in a 2 mm  $\times$  2 mm (4347  $\times$  4347 pixels) field of disks. Equation (B1) was applied to ten regions, and the results summed and fitted with high-order polynomials to find  $S(k)$ .

#### D. Form factor

We now estimate ESD by comparing measured and modeled backscatter coefficients as shown in Eq. (6).<sup>10</sup> The original method further reduced the MBSC( $k$ ) and  $\sigma_b(k)$  spectra to eliminate all frequency-dependent influences except for that caused by finite-size scatterers near  $ka = 1$ .<sup>8</sup> These reduced spectra are the scattering *form factors* defined as the Fourier transform of the spatial correlation function of  $f'$ . In the Results section, Sec. III, we show measured and modeled form factors as a means of interpreting ESD measurement errors.

#### E. Modeling fields of 2-D structures

Our simulation study progressed in stages to control for sources of ESD measurement error. First, the accuracy and precision of the ESD measurement technique were verified using sparse and dense monodisperse disks. Then the roles of size variability and compound scatterer structures on ESD measurements were examined. Once the influences of number density and size diversity were individually explored under controlled conditions, we studied 2-D histological images of healthy and fatty liver (FL) samples. Details of each echo simulation are given below.

##### 1. Scattering from monodisperse disks

We first generated 2-D fields of non-overlapping, *randomly positioned, identical, disk scatterers*. Figure 1(a) illustrates a 30- $\mu$ m-diameter fluid disk positioned within a fluid medium. ESD estimates are generated (Sec. II C) from broadband echo data simulated from fields of these disks (Sec. II B). The scattering model for a fluid disk is a 2-D version of the 3-D fluid-sphere model introduced by Anderson<sup>22</sup> and adopted in our work.<sup>8</sup> The term “fluid” refers to simple monopole/dipole scattering without shear-wave mode conversion. Random fields of weak scatterers<sup>31</sup> contain on the order of 5–10 disks per 2-D pulse area, which is dense enough to generate “fully developed” speckle in a sonogram but sparse enough to assume phases of echoes generated by disk scattering and received at the transducer surface are approximately uniformly distributed between 0 and  $2\pi$ . The result is incoherent scattering from the 2-D equivalent of a cloud of scatterers.<sup>12</sup> Increasing the disk number density, we were able to gradually increased the coherent scattering contribution from the same 30- $\mu$ m fluid disks.

The  $\gamma$  function from a disk of radius  $a$  with acoustic impedance  $z$  inside the disk and  $z_0$  outside the disk is

$$\gamma(r; a) = \begin{cases} 2z_0/z - 2 & \text{if } 0 < r \leq a \\ 0 & \text{if } r > a, \end{cases} \quad (9)$$

where  $r$  is radial position in the sound field relative to the disk center [Fig. 1(a)]. To mimic cell properties, we assume weakly scattering disks, i.e.,  $z_0/z \simeq 1$ , of diameter  $2a = 30 \mu\text{m}$  and  $z_0, z = 1.5, 1.7 \text{ MRayl}$ . (See Appendix A for details about transferring histology images to impedance maps.)

Applying Eq. (9) to Eq. (3) we find the modeled backscatter coefficient,

$$\begin{aligned} \sigma_b(k; a) &= 4\bar{n}k^3 \left( \left( \frac{z_0}{z} - 1 \right) \frac{a^2 J_1(2ka)}{2ka} \right)^2 \\ &= \bar{n}k^3 a^4 \gamma^2(r; a) \left( \frac{J_1(2ka)}{2ka} \right)^2, \end{aligned} \quad (10)$$

where  $J_1(\cdot)$  is a first-order Bessel function. Our observations of MBSC from these scattering media shown in the Results, Sec. III, suggest an area fraction of non-overlapping disks less than 10% may be considered random with minimal coherent scattering. The criterion for this assessment is a structure function that is approximately unity over the measurement bandwidth (discussed below). For area fractions greater than 10%, there is an increasingly significant coherent-scattering contribution not accounted for by  $\sigma_b$ .

##### 2. Scattering from random polydispersed disks

We studied randomly positioned fluid disks with a *distribution of diameters* about a mean diameter of 30  $\mu\text{m}$ , e.g., Fig. 1(b).<sup>25</sup> We also considered random fields of disks drawn from a narrow, normal probability density function (pdf) of diameters,  $2a \sim \mathcal{N}(\mu, \sigma^2)$  truncated to ensure  $a > 0$ . For example, Fig. 1(b) illustrates a normal distribution of disk diameters where  $30 \pm 9 \mu\text{m}$  and the ratio of standard deviation to mean is  $\sigma/\mu = 0.3$ . Incoherent scattering from a random field of polydispersed disks<sup>25</sup> gives  $\sigma_b$  as a sum of echoes from disk area density  $n_j$  at radius  $a_j$ ,

$$\sigma_b(k; a) = k^3 \sum_j \bar{n}_j a_j^4 \gamma^2(r; a_j) \left( \frac{J_1(2ka_j)}{2ka_j} \right)^2. \quad (11)$$

In Sec. III A, we test the approximation to Eq. (10) given in when disk size is distributed. We show it provides estimates consistent with Eq. (11) for  $\sigma/\mu < 0.5$ .

##### 3. Scattering from concentric disks

Random fields of *concentric fluid disks*<sup>23</sup> were investigated. Figure 2(a) illustrates one 10- $\mu$ m-diameter disk positioned concentrically within a 30- $\mu$ m-diameter disk, while Fig. 2(b) illustrates a 2-D random field of these compound structures.

For the weakly scattering concentric disks illustrated in Fig. 2,

$$\gamma(r) = \begin{cases} 2z_0/z_1 - 2 & \text{if } 0 < r \leq a_1 \\ 2z_0/z_2 - 2 & \text{if } a_1 < r \leq a_2 \\ 0 & \text{if } r > a_2. \end{cases} \quad (12)$$

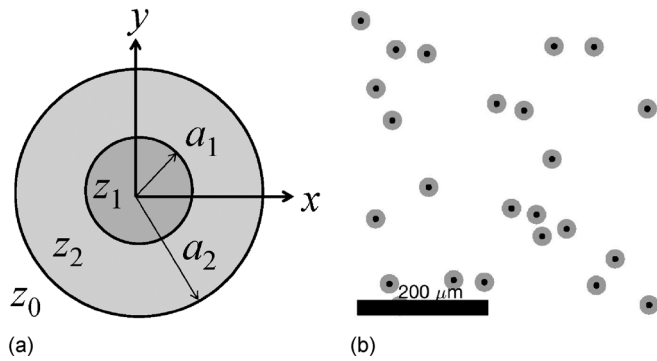


FIG. 2. 2-D impedance maps were simulated using random placements of discrete fluid-disk scatterers to validate the acoustic measurements. (a) Concentric fluid disks of radii  $a_1$  and  $a_2$  have corresponding impedance values  $z_1$  and  $z_2$ . (b) Simulated impedance field where 10- $\mu\text{m}$  disks locations are concentrically placed within 30- $\mu\text{m}$  disks.

We set  $2a_1, 2a_2 = 10, 30 \mu\text{m}$  and  $z_0, z_1, z_2 = 1.5, 1.7, 1.6 \text{ MRayl}$  to simulate scattering from cell structures. The corresponding backscatter coefficient is

$$\sigma_b(k; a_1, a_2) = 4\bar{n}k^3 \left( \left( \frac{z_0}{z_1} - \frac{z_0}{z_2} \right) \frac{a_1^2 J_1(2ka_1)}{2ka_1} + \left( \frac{z_0}{z_2} - 1 \right) \frac{a_2^2 J_1(2ka_2)}{2ka_2} \right)^2. \quad (13)$$

Notice  $\sigma_b$  is now parameterized by two diameters,  $2a_1$  and  $2a_2$ . For compound scatterers such as concentric disks, size parameter  $a$  in Eq. (7) becomes a vector,  $\mathbf{a} = \begin{pmatrix} a_1 \\ a_2 \end{pmatrix}$ , as indicated by Eq. (13). Now the objective function undertakes an exhaustive 2-D search for two parameters.

#### 4. Histology and impedance maps of rabbit liver

High-resolution microscopy images of rabbit-liver histology are used to model 2-D tissue scattering. The assumption is that cellular structures absorb histological stains during slide preparation in proportion to their protein or nucleic acid concentration that also determines the acoustic impedance of a structure. 3-D histology images were

successfully applied in an echo data simulator to provide acoustic signatures similar to those measured experimentally in 3-D living tissues.<sup>32</sup> The current study examines 2-D histology as a computationally efficient method for identifying cellular structures described by acoustic ESD estimates; we are not attempting to simulate the experimental tissue scattering results that were the focus of previous studies.<sup>32–34</sup>

Liver samples were extracted at necropsy, chemically prepared with formalin and sliced on a microtome into 3  $\mu\text{m}$  layers. Each sample is stained using hematoxylin and eosin (H&E) to indicate the distribution of protein structures in the slice plane.<sup>32</sup> Hemalum is taken up by cell nuclei, while eosinophilic structures, primarily cell membranes and fibers, are stained in proportion to their protein concentration. Each histology sample was imaged and digitized using a NanoZoomer HT slide scanner (NanoZoomer 2.0-HT; Hamamatsu, Hamamatsu City, Japan) sampled to give 0.46  $\mu\text{m}/\text{pixel}$ . The red and blue channels of the red-green-blue (RGB) microscopy image, which contain all the relevant information, were combined into gray-scale images. The red and blue channels of each pixel in the histology images were converted to impedance (2-D Z maps) using a methods described by Mamou *et al.*<sup>32</sup> and summarized in Appendix A. In Sec. III D, we evaluate the utility of applying the extra step of using impedance maps in echo simulation versus direct use of histology maps.

Liver histology from two groups of New Zealand white rabbits were examined: healthy and FLs.<sup>35</sup> Examples of the histology from both are shown in Fig. 3. FL cells are characterized by an accumulation of weakly staining lipids within hepatocytes (steatosis) that increase the average cell size and can displace the nuclei toward the cell wall. FL samples were obtained from rabbits fed a fatty diet for six weeks, while healthy liver tissue samples were obtained from a control group fed a healthy high-fiber diet.

The greatest distances between opposing cell walls and nuclear boundaries were measured optically along the vertical and horizontal image axes. Sizes of both structures were averaged for 100–120 of each cell type to set ground truth for ESD measurement comparisons. Healthy hepatocytes were found to have an average diameter of  $25.1 \pm 3.5 \mu\text{m}$ , while FL hepatocytes were 20% larger swelling to  $30.9 \pm 4.9 \mu\text{m}$ .

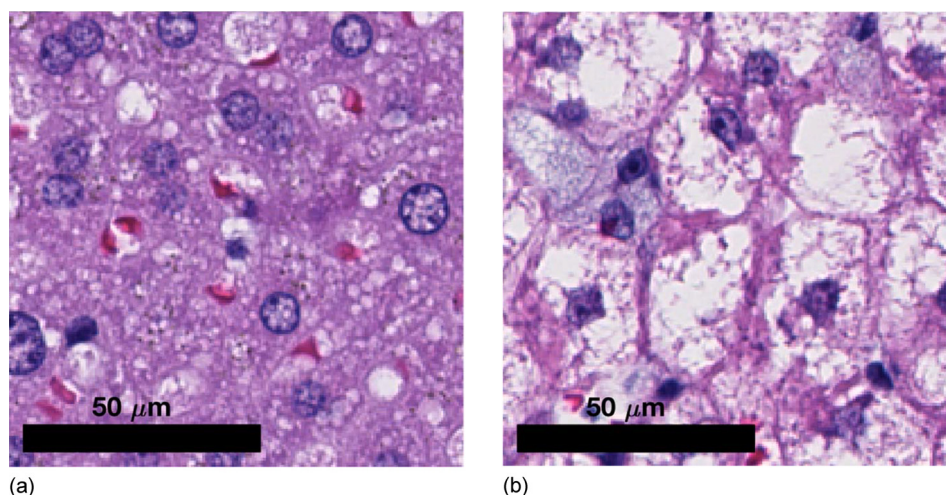


FIG. 3. (Color online) Images of rabbit liver histology. Image (a) is an example of a healthy liver while (b) is a FL. The scale bar indicates 50  $\mu\text{m}$ .

Healthy liver-cell nuclei were estimated to be  $9.5 \pm 1.5 \mu\text{m}$ , a value slightly (but not significantly) larger than the value  $8.7 \pm 1.4 \mu\text{m}$  found for FL liver cell nuclei. Since the images are of 2-D slices through 3-D tissue structures, average *in vivo* sizes are likely to be somewhat larger than values listed here.

## F. KL decomposition

Disk scatterers in the calibration studies are well defined discrete structures. However, cells and nuclei in tissue histology are more complex. Histology slides are formed from slices through cell bodies that present variable distributions of whole and partial somatic structures. Because ESD measurements are most sensitive to structures of size near the center wavelength of the pulse,<sup>7,17</sup> we need a method of sorting through cell histological structures. By systematically eliminating elements while comparing ESD estimates, we can identify the most influential scattering structures from histology.

For this task we apply the Karhunen-Loève (KL) decomposition of the spatial covariance matrix of histology data,  $\Sigma_f$ . It is known that sonographic brightness is determined by the properties of  $\Sigma_f$  (Ref. 27) that capture information about impedance correlations. To estimate  $\Sigma_f$ , we subdivided sampled large-field images of object scattering functions  $f'[p, q]$  as shown in Fig. 4. This original  $P \times Q$  matrix of real values, i.e.,  $\mathbf{f}' \in \mathbb{R}^{P \times Q}$ , is divided into  $B \times B$  blocks. Each block is lexicographically reordered into an  $M \times 1$  column vector, where  $M = B^2$ . Repeating this process for all  $N$  blocks in the original matrix  $\mathbf{f}'$ , we form a reordered matrix of the same echo data,  $\mathbf{f} \in \mathbb{R}^{M \times N}$ .

Let  $\bar{\mathbf{f}}$  ( $\mathbf{f}$  bar) be a  $1 \times N$  row vector of average impedance values, where the  $n$ th element is the mean value in the block corresponding to a column in  $\mathbf{f}$ , i.e.,  $[\bar{\mathbf{f}}]_n = \bar{f}_n = (1/M) \sum_{m=1}^M f_{nm}$ . Further let  $\tilde{\mathbf{f}}$  ( $\mathbf{f}$  tilde) be an  $M \times N$  matrix equal to  $\mathbf{f}$  except that  $\bar{f}_n$  has been subtracted from each value in the  $n$ th column, i.e., for the  $n$ th column  $[\tilde{\mathbf{f}}]_n = [f]_n - \bar{f}_n$ . This process subtracts the block mean from the impedance data in the corresponding block.

The spatial covariance matrix  $\Sigma_{f_n}$  for the  $n$ th block of the impedance map is defined as the ensemble average of the outer product of each of the  $N$  column vectors  $\Sigma_{f_n} = E\{([\mathbf{f}]_n - \bar{f}_n)([\mathbf{f}]_n - \bar{f}_n)^T\}$ , where superscript  $T$  denotes matrix transpose. For wide-sense stationary media,

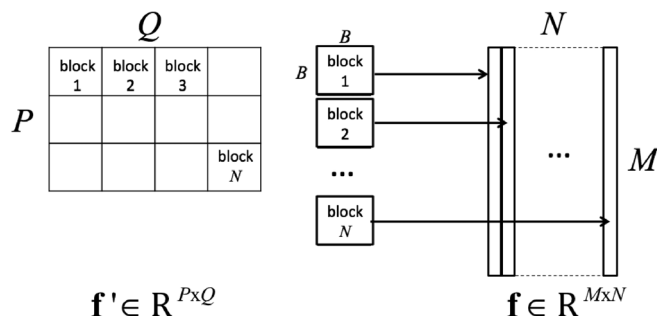


FIG. 4. The impedance map is represented by  $P \times Q$  matrix  $\mathbf{f}'$ . It is reshaped into  $M \times N$  matrix  $\mathbf{f}$  for use in Eq. (14) to compute the covariance matrix. Data “blocks” are given by the columns of  $\mathbf{f}$ .

covariance matrices for all blocks are approximately equal. Therefore, we can apply the practical approximation via spatial averaging,

$$\Sigma_f \simeq \tilde{\mathbf{f}} \tilde{\mathbf{f}}^T, \quad (14)$$

provided the two assumptions hold true. First,  $\mathbf{f}$  must be a stationary random process where spatial averaging over blocks closely approximates ensemble averaging (ergodicity). Second, we must be willing to limit the analysis to tissue structures on the size of the block and smaller. For example, the  $100 \times 100$  pixel block size used in our study limits backscattered echoes to structures smaller than  $46 \mu\text{m}$  (with pixel size of  $0.46 \mu\text{m}$ ), on the order of the cell size. These are reasonable assumptions for our analysis purposes. Please note that inter-cellular structures can contribute to the simulated echo signal, necessitating use of the structure function in Eq. (7), but were not a factor in object decomposition and filtering described below.

The KL expansion of  $\Sigma_f$  (equivalent to principal-component analysis (PCA) or Hotelling transformation<sup>36</sup>) is conveniently obtained using eigenanalysis,<sup>37</sup>

$$\Sigma_f = \mathbf{D} \mathbf{V} \mathbf{V}^T. \quad (15)$$

$\mathbf{D}$  is a diagonal matrix of the eigenvalues of  $\Sigma_f$  sorted in descending order, and  $\mathbf{V}$  is a matrix where columns are the corresponding eigenvectors. For a  $100 \times 100$  block size,  $\mathbf{D}$  and  $\mathbf{V}$  are each  $M \times M$ , where  $M = 10^4$ . The KL transformation of  $\tilde{\mathbf{f}}$ , labeled  $\mathbf{y}$ , is another  $M \times N$  matrix,

$$\mathbf{y} = \mathbf{V}^T \tilde{\mathbf{f}}. \quad (16)$$

Combining Eqs. (14)–(16), we find  $\mathbf{y} \mathbf{y}^T = \mathbf{D}$  where  $y_m^2 = D_{mm}$  are the eigenvalues of  $\Sigma_f$ .

Scattering structures can be systematically discarded by setting some eigenvalues to zero. For example, we find  $\mathbf{y}_j$  by setting  $D_{mm} = 0$  for  $j + 1 \leq m \leq M$  to reduce the rank of  $\Sigma_f$ . Applying the inverse KL transformation

$$\tilde{\mathbf{f}}_j = \mathbf{V} \mathbf{y}_j \quad (17)$$

and adding  $\bar{f}_n$  to matrix columns with nonzero eigenvalues we find  $\mathbf{f}_j$ . The reduced impedance map,  $f'_j$ , is a reshaped version of  $\mathbf{f}_j$  computed by reversing the process outlined in Fig. 4 via the reshape MATLAB function (MATLAB and Statistics Toolbox, The MathWorks, Inc., Natick, MA).

We vary threshold index  $j$  from  $M$  (no reduction in scattering structure) to 1 (max reduction) to discard increasing amounts of the tissue impedance structure, generally from the finest structures to the coarsest, with minimal distortion of the remaining components.<sup>38</sup> We then apply map  $\mathbf{f}'_j$  in echo simulations as described Sec. II B. As  $j$  varies and ESD values change, we can infer the influence of lost structures on the shape of the echo spectrum. At any point in the analysis, computing  $\mathbf{f}'_{M-j-1}$ , i.e., zeroing the first  $j$  eigenvalues of  $\Sigma_f$ , allows visualization of the structures that have been removed from the histology or Z maps, e.g., Figs. 12(b) and 12(e).

We keep track of the discarded structures through two quantities. First, percent eigenenergy is defined via Eq. (18) to be

$$E = \frac{\sum_{m=1}^j y_m^2}{\sum_{m=1}^M y_m^2} \times 100, \quad \text{where } 1 \leq m \leq M \quad (18)$$

and  $j$  is a threshold integer. The discarded eigenenergy percentage is  $100 - E$ . We used a data block size of  $100 \times 100$  so there are always  $M = 10^4$  eigenvalues. The second quantity that we track is  $j$ , the number of eigenvalues included in the scattering object for the range  $1 \leq j \leq M$ . The number of discarded eigenvalues is  $M - j$ .

### III. RESULTS

#### A. Disk-scatterer calibrations

For the disk scatterers described in Sec. II E, we simulated echo signals at pulse center frequencies up to 45 MHz (Sec. II B) and estimated ESD [Sec. II C, Eq. (7)] for sparse (7% area fraction) and dense (28% area fraction) disk fields. Each point in the plots of Figs. 5–7 is an average of ten simulations using statistically independent realizations of the random object data. The search range applied for the 30- $\mu\text{m}$  disks was set at 0–60  $\mu\text{m}$ ; all estimates for the ten trials fell inside this range. Error bars indicate  $\pm 1$  standard error for  $N = 10$ . For all results, the fractional pulse bandwidth was fixed at 58%; consequently, for example, 15 MHz pulses have three times the bandwidth of 5 MHz pulses.

##### 1. Sparse monodisperse disks

ESD estimates for sparse random fields of 30- $\mu\text{m}$ -diameter disks are shown in Fig. 5(a). The horizontal dotted line is the diameter of the disks in the object function used to simulate echo signals. The dashed and solid curves are ESD estimates with and without the structure function correction, respectively. Estimates are obtained without the structure function by setting  $S(k) = 1.0$  in Eq. (8). The central frequency of the pulse indicated on the lower horizontal axis is matched to the corresponding values of  $ka$  on the upper axis. Results with and without the structure function agree above 10 MHz, suggesting the medium is random with minimal coherent scattering contributions when the disk density is set to a 7% area fraction. The structure function tends to bias ESD estimates high at pulse frequencies below 10 MHz.

The error bars indicate ESD estimates are precise for ten trials when  $ka > 0.8$ . Generally, estimates are expected to be most accurate with  $ka$  from 0.8 to 1.<sup>7,17</sup> However, the lack of fine-scale structural information within disks allows a fluid-disk model to well represent this scattering medium even at higher frequencies. For  $0.8 < ka < 1$ , uncorrected ESD estimates [ $S(k) = 1$ ] range from 30  $\mu\text{m}$  to 29.2  $\mu\text{m}$ . For  $ka > 1.2$ ,  $\text{ESD} \approx 31 \mu\text{m}$ . These results validate the method for measuring ESD from 2-D echo data.

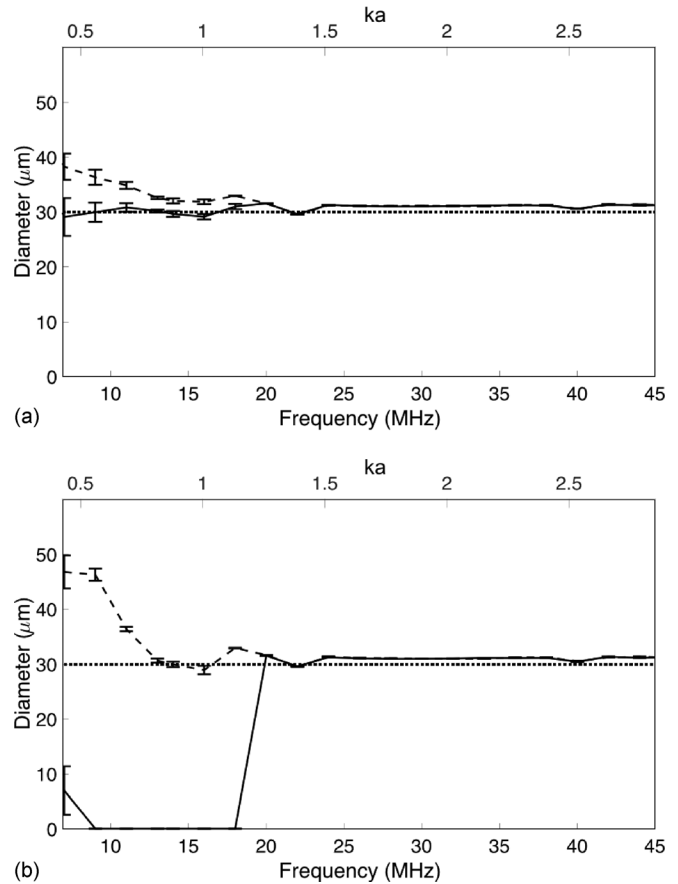


FIG. 5. (a) ESD estimates from a sparse (7% area fraction) field of 30- $\mu\text{m}$  fluid disks. (b) ESD estimates from a dense (28% area fraction) field of 30- $\mu\text{m}$  fluid disks. Solid and dashed line are ESD estimates before and after structure function correction, respectively. The dotted line indicates the simulated disk diameter. Estimates are made for center pulse frequencies between 7 and 45 MHz; the corresponding values of  $ka$  are listed on the upper horizontal axis.

##### 2. Dense monodisperse disks

Repeating the study above for fields of 30- $\mu\text{m}$ -diameter disks having a 28% area density, we find the results of Fig. 5(b). The dashed and solid lines are ESD estimates with and without the structure function correction, respectively, as in Fig. 5(a). The solid line indicates that effects of coherent scattering appear strongest in the long-wavelength limit at  $ka < 1.2$ . In this range, the model almost completely failed to represent the echo spectrum. These effects indicate that dense media cannot be considered random as coherent scattering influences are significant. Application of the structure function allows use of the backscatter coefficient models for random media in Eqs. (2), (3), and (5). Corrected estimates (dashed line) compensate the spectrum for coherent scattering and, as a result, ESD measurements match values obtained from sparse random fields above 12 MHz. Again, for  $ka < 0.8$ , the structure function biases ESD estimates high.

##### 3. Sparse polydisperse disks

This section explores the influence on ESD estimates of a narrow size distribution of sparse disk scatterers. Equation (10)

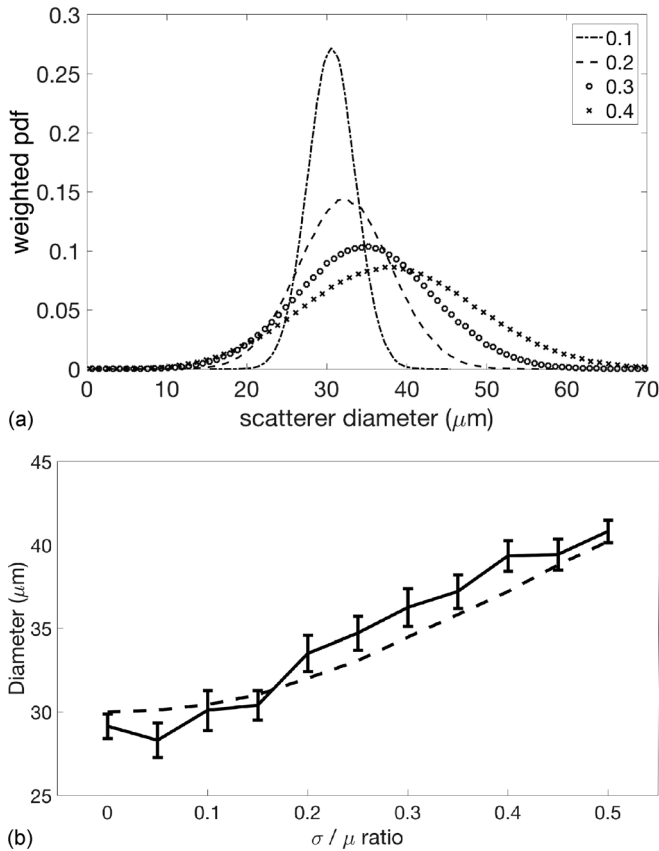


FIG. 6. (a) Weighted normal probability densities  $p(2a) \times (2a/\mu)^2$  for fluid-disk scatterers. Although  $\mu = 30 \mu\text{m}$ , the quadratic factor shifts the weighted mean from  $30 \mu\text{m}$  to  $40 \mu\text{m}$  as  $\sigma/\mu$  increases from 0.1 to 0.4. The legend indicates the ratio of diameter standard deviation to mean for each curve. (b) The solid line indicates ESD measurements versus  $\sigma/\mu$  for a 16-MHz pulse. The dashed line indicates the predicted results based on the weighted probability model.

shows disks are weighted by the fourth power of the radius, suggesting that to first order, ESD estimates are biased by the width of the diameter distribution. Referring to the monodispersed disk data of Fig. 5(a) at 16 MHz ( $ka \approx 1$ ), we find  $\text{ESD} = 29.2 \pm 0.5 \mu\text{m}$  for a random field of exactly  $30\text{-}\mu\text{m}$  disks. This value becomes the measurement in Fig. 6(b) at standard-deviation-to-mean ratio  $\sigma/\mu = 0.0$ . Measurements from simulated echo data at other values of  $\sigma/\mu$  indicate that broader distributions are indeed biased higher.

We found a simple way to predict ESD bias from the size distribution. Figure 6(a) shows four weighted, normal distributions of scatterer diameters, i.e.,  $2a \sim \mathcal{N}(\mu, \sigma^2)$ , each with different  $\sigma/\mu$  ratios and all with a fixed mean of  $30 \mu\text{m}$ . However, these probability densities are multiplied by the factor  $(2a/30 \mu\text{m})^2$  at each diameter value as predicted by the  $\sigma_b$ . We see from Eqs. (11) and (13) that  $\sigma_b$  is proportional to  $k^3 a^2$  for cylinders.<sup>12</sup> However  $\sigma_b$  is proportional to  $k^4 a^3$  for spheres,<sup>8,12</sup> showing the model must be adjusted when using 2-D versus 3-D scattering fields in the simulations. The predicted influence on ESD measurements from a diameter distribution is shown by the dashed line in Fig. 6(b) while the corresponding measurements from echo signals simulated using polydisperse disks is shown by the solid line. This coarse approximation is reasonably predictive for

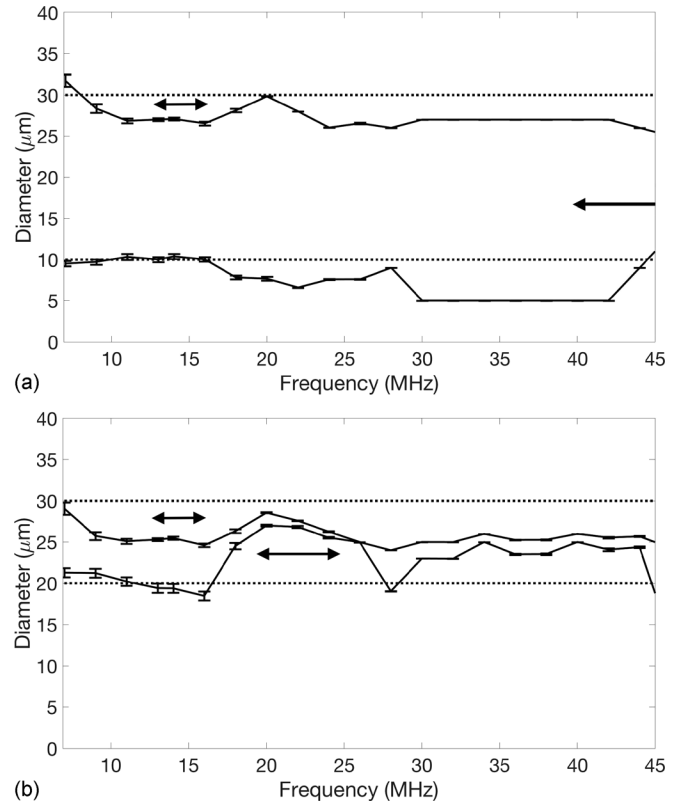


FIG. 7. (a) ESD estimates are obtained from sparse 2-D fields of  $10\text{--}30\text{-}\mu\text{m}$ -diameter concentric disks, coarsely representing incoherent scattering from liver cells and their nuclei. (b) ESD estimates are obtained from sparse 2-D fields of  $20\text{--}30\text{-}\mu\text{m}$ -diameter concentric disks. Error bars are standard errors for ten trials made at pulse frequencies in the range  $7\text{--}45$  MHz. The horizontal arrows indicate frequency ranges where  $0.8 < ka < 1$ .

$0 \leq \sigma/\mu \leq 0.5$ , which includes the observed variability among fatty and healthy liver cells seen histologically.

#### 4. Sparse concentric disks

ESD estimates for randomly positioned concentric-disk scattering fields are summarized in Fig. 7. Clearly the added structural complexity challenges the accuracy of this estimator. We applied the two-parameter backscatter coefficient model from Eq. (13) and the two-parameter search via the measurement approach in Eq. (7) to find these results. In Fig. 7(a), the ratio of outer- to inner-disk diameter is larger than a factor of 2 ( $30$  and  $10 \mu\text{m}$ ), and in Fig. 7(b) it is smaller than a factor of 2 ( $30$  and  $20 \mu\text{m}$ ). The search range for the outer disk was set to  $20\text{--}40 \mu\text{m}$ , while that for the inner disk was  $5\text{--}30 \mu\text{m}$ . Search ranges were selected to reduce the computational load without biasing ESD estimates. Each point in the plots of Figs. 7(a) and 7(b) is an average of at least 10 trials drawn from 25 to 50 simulations of random object data. Out-of-range searches were labeled as failed and excluded from the average values plotted. Error bars indicate  $\pm 1$  standard error for  $N=10$ . Extra simulations were needed to obtain at least ten estimates within the search ranges of the smaller disk.

Arrows in Figs. 7(a) and 7(b) indicate the  $0.8 < ka < 1.0$  ranges for the  $10\text{--}30\text{-}\mu\text{m}$ - and  $20\text{--}30\text{-}\mu\text{m}$ -diameter compound-disk scatterers. When the ratio of outer-to-inner diameters is greater

than 2, as in Fig. 7(a), the estimator recognizes that two disk sizes are present, even though both estimates are less accurate when compared with scattering from fields of simple disks. However, when the ratio of outer-to-inner diameters is less than 2, as in Fig. 7(b), ESD estimates tend to merge at frequencies above 18 MHz as the 2-D search for the optimal  $a_1, a_2$  pair does not provide distinct estimates. Note that  $ka_1 = 1$  for the  $10\ \mu\text{m}$  disk at 49 MHz, which makes the accurate  $10\ \mu\text{m}$  estimates below 16 MHz surprising and unreliable. We further examined the effect of randomizing the location of the inner disk within the outer disk (coincident but not concentric). We found results (not shown) that are essentially equivalent to those of the concentric disks found in Fig. 7.

Although the concentric-disk model shows some separability of the compound disks, we found no benefit in applying a simultaneous 2-D search for  $a_1$  and  $a_2$  as compared to performing separate 1-D searches with single-disk models.

### 5. Summary of calibration studies

Overall, the calibration results from Figs. 5–7 suggest that ESD estimates can accurately represent monodisperse structures for  $ka > 0.8$ . As the true distribution of scatterer sizes increases, ESD estimates depend on both the mean and standard deviation of the distribution. Given some prior knowledge of scatterer distributions, the effects of the size distribution can be accounted for. When there is more than one distinct size distribution, these structures can be separately assessed with appropriate selection of pulse frequencies provided scatterer sizes vary by at least a factor of 2. Objects with sizes within a factor of 2 generate ESD estimates somewhat larger than the average object size, which can be predicted by applying an acoustic weighting factor. Determining the size of  $10\text{-}\mu\text{m}$ -diameter disks is very challenging below 45 MHz using a fluid disk model. Finally, when the area fraction of scatterers is larger than about 10%, ESD estimation accuracy is greatly improved with use of the

structure function to reduce coherent scattering effects on the backscattered spectrum.

### B. ESD for healthy liver and FL histologies

Based on the calibration results of Sec. III A, we now consider ESD measurements made by processing echoes simulated from liver histology images. ESD results for healthy and FL data in Fig. 8(a) show subtle differences with overall trends that vary significantly between 9 and 45 MHz. The error bars for data in Fig. 8(a) are too small to see clearly, so we replotted a portion of the data near  $ka \simeq 1$  in Figs. 8(b) and 8(c) to show that error bars are minimum near  $ka \simeq 1$ . Error bars indicate  $\pm 1$  standard error from estimates made on three disjoint tissue regions. The structure function correction is applied to all of the tissue histology data shown.

Section II E described light-microscopy measurements of cell diameters where we found healthy rabbit hepatocytes to be  $25.1 \pm 3.5\ \mu\text{m}$ . The calibration studies from Fig. 6 using polydispersed random disk media predicts ESD estimates for healthy liver cells should be biased high at  $26\ \mu\text{m}$  due to the narrow distribution of cell sizes ( $\sigma/\mu = 0.14$ ). ESD estimates from echo simulations in Fig. 8(b) gives  $26.4\ \mu\text{m}$  at 18 MHz where  $ka \simeq 1$ , in close agreement with distribution adjusted optical histology measurements. Section II E also lists optical measurements that show FL hepatocytes have size  $30.9 \pm 4.9\ \mu\text{m}$ . Figure 6 data predict ESD estimates for these FL cells should be biased high at  $32\ \mu\text{m}$ . The ESD estimate in Fig. 8(c) is  $31.5\ \mu\text{m}$  at 15 MHz where  $ka \sim 1$ , also in close agreement. Looking blindly over the data in Fig. 8(a), one is hard pressed to clearly say ESD is able to discriminate healthy and FLs. However, liver histology is reasonably consistent within a species, and so it should be possible to select a pulse frequency near  $ka = 1$  that targets the size of hepatocytes expected for a population. Because cell and nuclear sizes are different by more than a

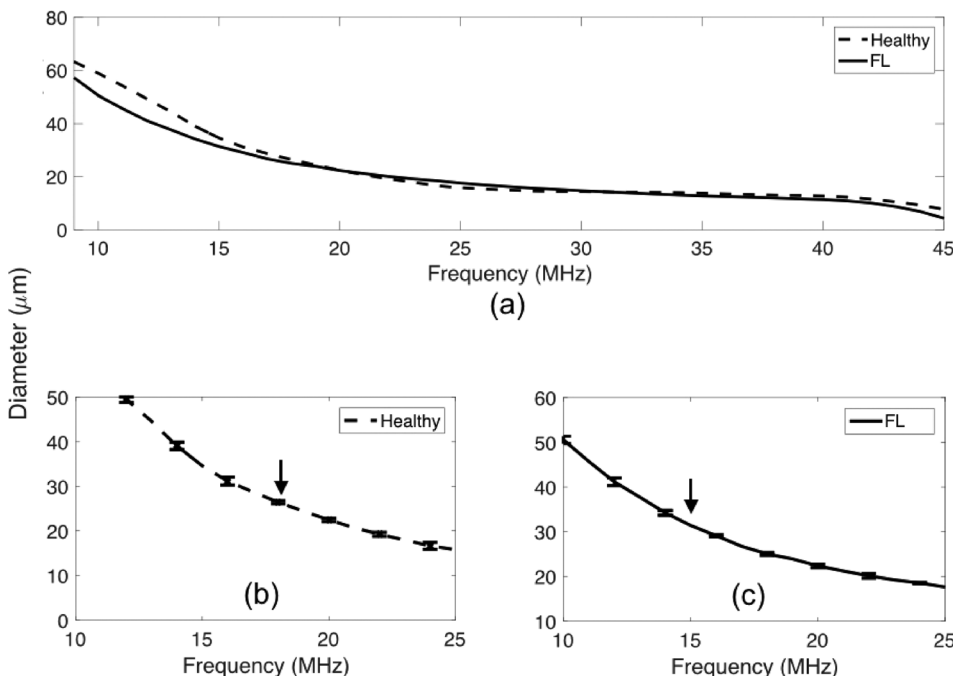


FIG. 8. (a) ESD estimates from healthy and fatty rabbit liver histologies at pulse frequencies between 9 and 45 MHz. (b),(c) ESD estimates from both liver types in (a) are magnified to show how the error bars are minimum near  $ka \sim 1$  (arrows).

factor of 2, echoes from these structures are not expected to interfere in ESD measurements.

Estimating nuclear sizes is more difficult than estimating cell sizes, which was predicted by the calibration results. At roughly  $9\ \mu\text{m}$ ,  $ka = 1$  for cell nuclei near a pulse center frequency of 50 MHz. For a fixed 58% fractional bandwidth, we need to sample echo signals at rates above 150 MHz to avoid aliasing. Even more limiting is the high acoustic attenuation that reduces the penetration depth needed if these measurements were made *in vivo*. Recall that our simulations did not include tissue attenuation or acquisition noise. The ESD estimates of nuclear size made at 40 MHz,  $ka = 0.73$ , were  $12.7\ \mu\text{m}$  for healthy hepatocytes and  $11.4\ \mu\text{m}$  for FL hepatocytes. The optical measurement of healthy cell nuclei is  $9.5 \pm 1.5\ \mu\text{m}$  and the distribution corrected value is  $9.8\ \mu\text{m}$ . The optical measurement of FL nuclei is  $8.7 \pm 1.4\ \mu\text{m}$  and the distribution corrected value is  $9.0\ \mu\text{m}$ . Although ESD measurements are about 30% higher than corrected optical values, the rank order of cellular and nuclear sizes is preserved.

### 1. Summary for tissue histology

ESD measurements from liver histology decrease with pulse frequency. Where  $ka \simeq 1$ , we find that ESD estimates of cell sizes closely agree with optical measurements of the average liver cell sizes if the measurements are adjusted for the histological distribution in cell diameters. ESD estimates of cell nuclear sizes are less accurate, generally biased about 30% high because of difficulties in achieving pulse frequencies where  $ka \simeq 1$ .

### C. Form factor

In each of the studies summarized by Figs. 5–8, we find that ESD estimates have high variance in the long-wavelength limit, i.e., at  $ka < 1$ . To explore sources of this uncertainty, we examine in Fig. 9 the relationship between measured and modeled acoustic form factors.

Notice that the variance in measured form factor values decreases with increasing frequency. Measured form factor

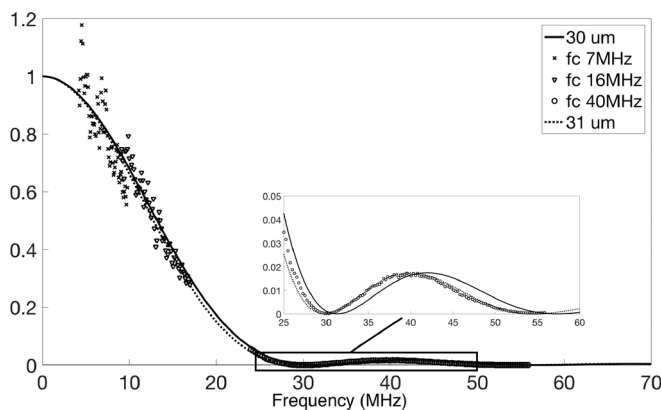


FIG. 9. Best fit form factor for the fluid disk with scatterer diameters of  $30\ \mu\text{m}$  and  $31\ \mu\text{m}$  are shown in solid and dotted lines, respectively. The form factors for echo data at pulse center frequency of 7, 16, and 40 MHz are calculated and scaled. Model form factors at  $2a = 30$  and  $31\ \mu\text{m}$  show how sensitive the models are to a  $1\text{-}\mu\text{m}$ -diameter difference.

uncertainty is determined by that of the echo-signal power spectral density on which they are based. We always simulated data over the same depth range so the frequency resolution is the same for all pulse frequencies between 7 and 45 MHz. Increasing the axial sampling rate for higher-frequency pulses extends the Nyquist frequency to reduce aliasing. However, none of these factors affect form factor uncertainty within the estimation bandwidth. That uncertainty is largely determined by the number of independent samples obtained across the lateral extent of the object, as explained in the discussion, Sec. IV.

### D. KL decomposition of liver-tissue structures

Given the complexity of tissue structures seen in Fig. 3, we found them difficult to classify using one or several probability distributions. To sort through them systematically, we first apply a KL decomposition of the histology images as described in Sec. IIF. This allowed us to “disassemble” and discard elements of cell structures. We then reassemble remaining components via Eq. (17), simulate echo signals, and observe the effects on ESD measurements. The largest eigenvalues of the tissue histology generally correspond to eigenvectors representing coarse structures, while the smallest eigenvalues correspond to fine-scale structures. While eigenvectors are not the sinusoids of a Fourier basis, the trends are similar.

In Fig. 10 we investigated the relationship between the number of eigenvalues included in the scattering object and eigenenergy percentage for both histology and impedance images computed from the liver tissues of Fig. 3. We find that the largest 20 eigenvalues of histology images (0.2% of  $10^4$  values over a  $46\text{-}\mu\text{m}$  scale) carry 10% of the eigenenergy, whereas the largest 500 eigenvalues carry 70% of the eigenenergy. Recognizable histological features are described by 70% of the eigenenergy in fewer than 5% of the eigenvalues.

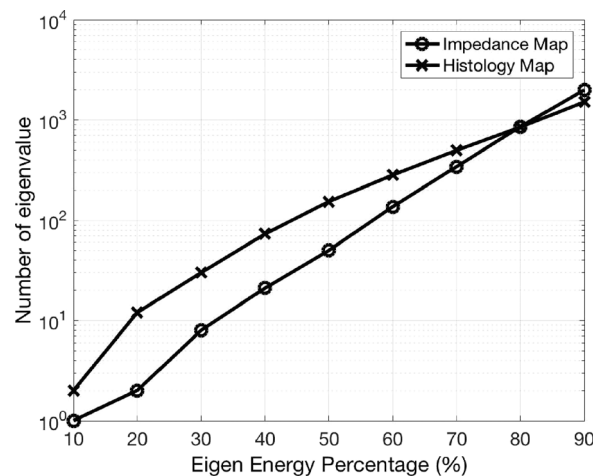


FIG. 10. Measurements of the change in the number of eigenvalues out of  $10^4$  as a function of eigenenergy for histology images undergoing KL decomposition. Results of analysis on histology images are compared with those for the same data converted into impedance maps. Curves show that the greater dynamic range of histology images over impedance maps (8 bits versus 3 bits) results in the same eigenenergy being distributed over more eigenvalues.

Converting histology data into impedance maps (see Appendix A) adds direct physical context to the object scattering field,  $f'$ . However impedance maps have a lower dynamic range compared with histology images (3 bits versus 8 bits) resulting in more eigenenergy being placed into fewer eigenvalues, as seen from Fig. 10. Finding no significant difference between ESD estimates using histology image data and impedance maps, we chose to use the former to preserve the dynamic range of  $f'$ .

Figure 11(a) displays ESD measurements versus eigenenergy for the two types of rabbit-liver histology. Measurements made at 18 MHz for healthy hepatocytes and at 15 MHz for FL cells keep  $ka \approx 1$ . Estimates are constant for eigenenergy values greater than 25%, varying only when  $E < 25\%$ . Measurements made at 40 MHz in Fig. 11(a) target cell nuclei for which  $ka \approx 0.73$ . ESD estimates at 40 MHz are constant when the eigenenergy is greater than 40%. The first changes we see below these thresholds are an increase in ESD estimates as the remaining scattering structures are blurred forms of histology. Further, we focused on one normal hepatocyte imaged at five eigenenergy levels in Fig. 11(b) and one fatty-liver cell at five eigenenergy levels in Fig. 11(c) so that readers can visualize the effects of eroding structures via the KL decomposition process.

The results of Fig. 10 show that fine-scale structures in cells have little influence on ESD estimates. The disk calibration studies show that for size differences greater than a factor of 2, viz., where  $ka < 0.5$  or  $ka > 2.0$ , we expect those structures to have little influence on ESD estimates. Further, we find that ESD measurements between 7 and 45 MHz are sensitive to only the largest 200–700 eigenvalues out of 10 000. In comparison, the disks in the calibration studies contained more than 90% of the eigenenergy in fewer than 100 eigenvalues. The rank of the spatial covariance matrix formed from liver-tissue scattering functions is fairly small, becoming still smaller once tissues are coupled to acoustic pulses in the range of 7–45 MHz. For this reason, selecting an ultrasonic pulse determines which specific tissue structures are sensed despite there being significant structural diversity.

#### IV. DISCUSSION

Notice in Fig. 9 that variance in measured form factor values decreases with frequency. Form factor uncertainty reflects that of the echo-signal power spectral density. Spectral uncertainty is largely determined by the number of independent samples averaged across the lateral extent of the object.

As pulse frequency increases, pulse length and width decrease for fixed bandwidth and  $f$ -number. However, the lateral sampling interval was fixed at 0.1 mm. Echo samples are more correlated along the lateral dimension at lower frequencies because the pulse volume is relatively larger. Significant correlation among waveforms at a fixed depth reduces the number of degrees of freedom available when averaging lateral samples over a fixed total lateral extent during spectral estimation. Also, since bandwidth scales with transmission frequency, low-frequency pulses provide fewer points in the

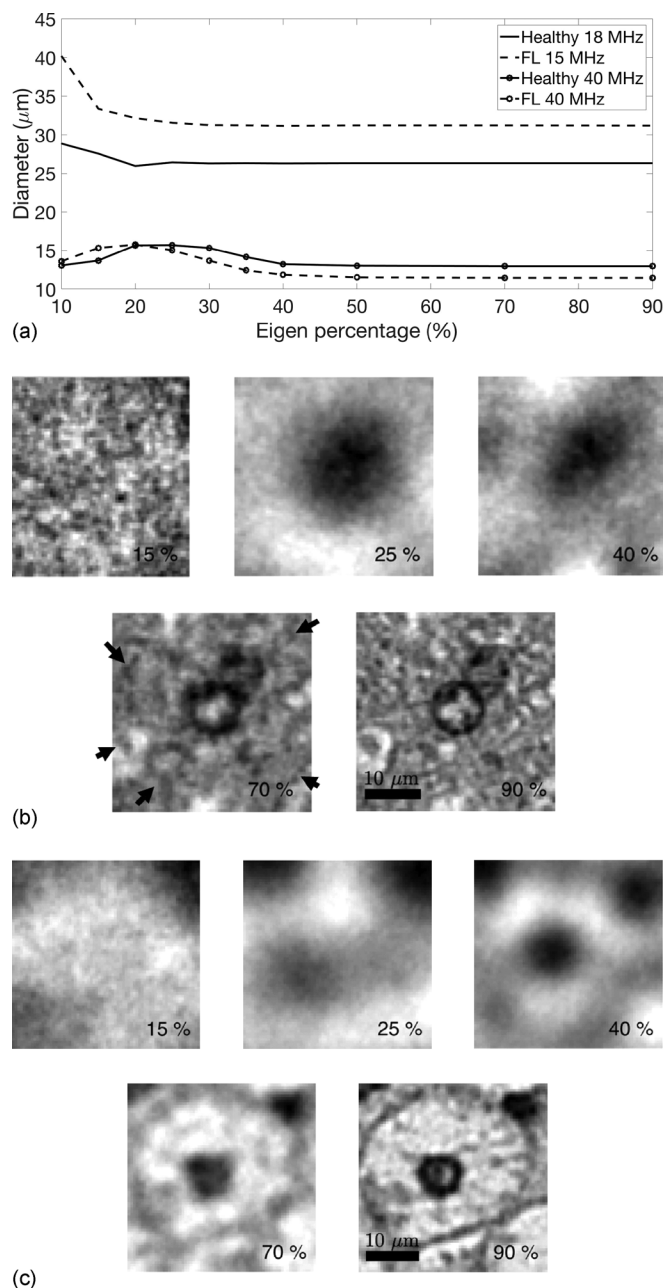


FIG. 11. (a) ESD estimates for healthy liver and FL histology maps as a function of the preserved eigenenergy. Healthy liver values are obtained using 15-MHz pulses while FL values are obtained at 18-MHz to focus on the cellular structures. 40 MHz pulses are applied for both healthy liver and FL to focus on nuclear structures. Hepatocyte images from healthy (b) and fatty (c) livers are reconstructed with 15% (top left), 25%, 40%, 70%, and 90% (lower right) of the total eigenenergy. In (b), arrows indicate the cell membrane.

ESD measurement bandwidth of Eq. (8). The combination of fewer bandwidth points and greater uncertainty at each point reduces the accuracy of ESD measurements at low pulse frequencies relative to high frequencies.

Figure 9 also explains why ESD estimates improve as pulse frequency increases for monodispersed disks when the modeled form factor well represents scattering in the medium. The combination of wide bandwidth and precise spectral estimates allows fluctuations in the model function to uniquely fit the data. In contrast, compound disks are not

well represented by the fluid-disk model function, and so ESD estimates are not accurately estimated at  $ka > 1$ .

Attenuation and noise were not included in our simulation in order to provide us with these specific insights. Patient measurements always involve frequency-dependent attenuation and acquisition noise, which reduce the echo signal-to-noise ratio (SNR) in clinical studies at high frequencies. To compromise, a pulse frequency near  $ka = 1$  should be selected based on *a priori* knowledge of the class of patient histology under investigation. Near  $ka = 1$ , one expects the combination of moderate echo SNR and high form-factor curvature to yield the most accurate and precise ESD measurements. The exact choice of form-factor model function limits ESD accuracy less than the presence of spectral noise in a narrow measurement bandwidth.

To the extent that liver can be described as a normally distributed ergodic process generating incoherent scattering fields, the spatial covariance matrix provides a complete representation of tissue structure.<sup>39</sup> These assumptions are

essential for straightforward interpretation of ESD results. KL decomposition also assumes the tissue scattering function  $f'$  is normally distributed. It diagonalizes the spatial covariance matrix, which decorrelates  $f'$ . The symmetry of every covariance matrix ensures that eigenvectors are orthogonal, but only if the scattering object is normally distributed can we also assume the eigenvectors are linearly independent. Cellular structures uncouple in this way only if  $f'$  can be expressed as a normal random process.

We examined the normality of histological data qualitatively by forming histograms of  $10^6$  image pixels from healthy liver and FL data; see Fig. 12. Although neither is normally distributed, clearly FL samples [Fig. 12(d)] deviate from normality more than healthy liver because of the large lipid content. In Figs. 12(b) and 12(e) we reconstructed images of 10% eigenenergy for the smallest eigenvalues that we expected to contain image noise. In Figs. 12(c) and 12(f) we blended the 10% eigenenergy images with the corresponding 100% eigenenergy images so that readers can see how some cell

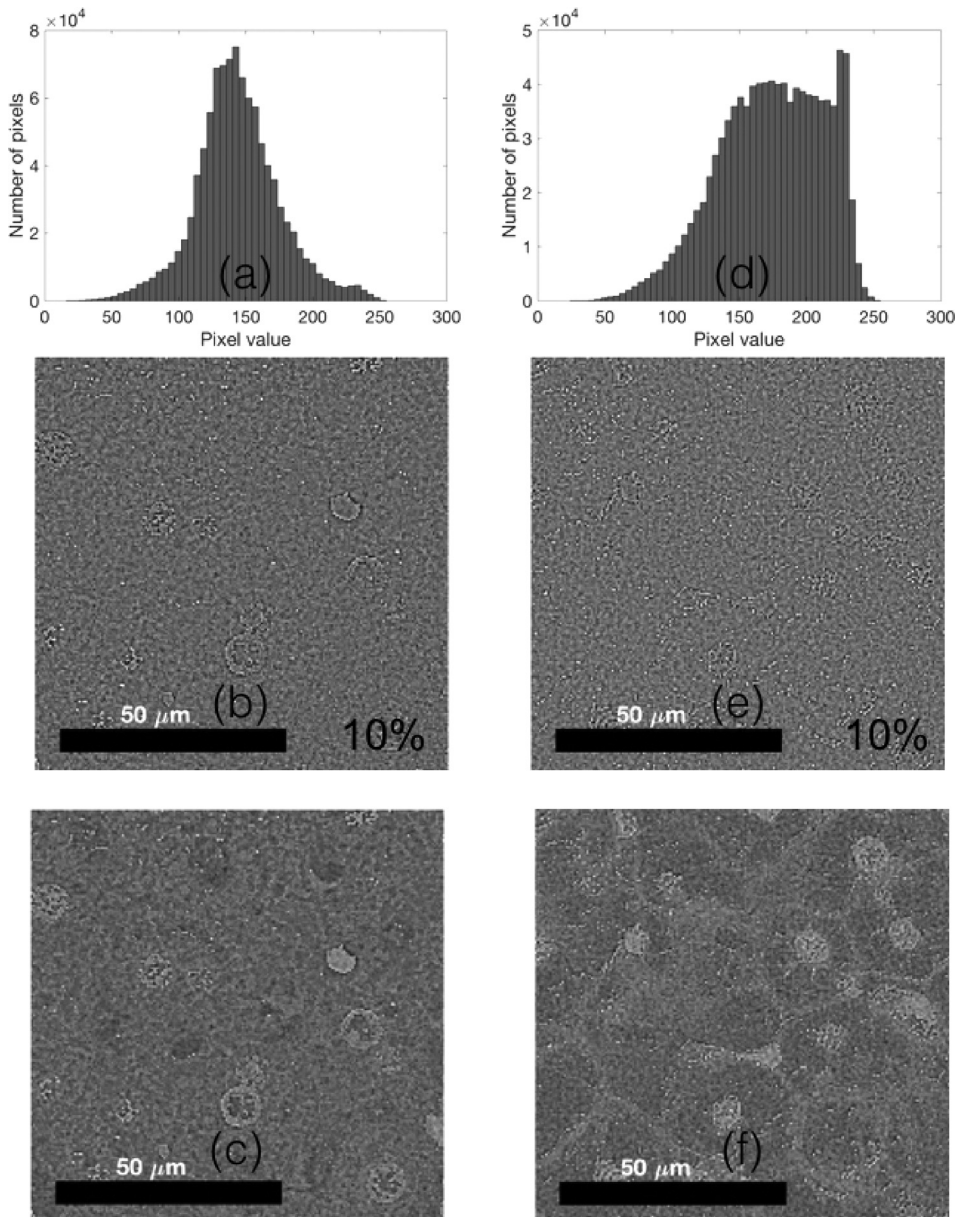


FIG. 12. (a) Histogram of the 8-bit gray-scale histology map for healthy liver. The total number of pixels included is  $10^6$ . (b) Reconstructed healthy liver histology using only the smallest 10% eigenenergy. (c) The result of (b) added in registration to the faded (20%) histology map of Fig. 3(a). Comparing (b) and (c) allows readers to visualize the discarded data in light of the original histology. (d) Histogram of the 8-bit gray-scale histology map for FL. The total number of histology image pixels included is  $10^6$ . (e) Reconstructed FL histology using only the smallest 10% eigenenergy. (f) The result of (e) is added in registration to the faded (20%) histology map of Fig. 3(b).

structures do completely uncouple. In particular, we see nuclei appearing in both images and a noticeable amount of the cell wall structure in the FL image of Fig. 12(f). These results show that the KL decomposition does not completely separate cell components from smaller structures and noise as we hoped. Nevertheless it does permit us to determine the rank of the object covariance matrix contributing toward ESD estimates. This was the point of data in Fig. 11(a).

Application of structure function  $S(k)$  in Eqs. (7) and (8) minimized the coherent scattering effects from dense media on the echo spectrum. Calibration results in Fig. 5(b) emphasized the importance of  $S(k)$  for ESD measurements at low frequencies.  $S(k)$  adjusts the echo spectrum when the phases from echoes combined at the transducer surface are not uniformly distributed. Wagner *et al.*<sup>31</sup> showed that uniform echo phase distributions are a hallmark of normally distributed echo signals,  $g$ .

We then computed structure function using the method of Han and O'Brien<sup>30</sup> via Eq. (B1) except that we fit  $S(k)$  results to an eighth-order polynomial to minimize phase noise. The goodness of fit is routinely poorer below 20 MHz where  $S(f)$  consistently overcorrects ESD estimates [see Fig. 5(a)]. Unlike in our simulations, exact locations of each reflecting scatterer are unknown *in vivo*, in which case  $S(k)$  is computed from statistical models of scatterer density.<sup>26</sup> We note that hepatocytes in the selected regions of this study are uniformly distributed with no vascular structures. Thus only the coherent scattering among hepatocytes is considered in our simulations. Eliminating highly reflecting arterioles allowed us to focus the analysis on cellular scattering, which is impossible experimentally in tissues.

Finally, we undertook this investigation in two dimensions to maintain realistic memory requirements and computational loads. The 2-D scattering geometry changes the backscatter models used in ESD estimation compared with 3-D analysis. We find no reason to expect lessons learned in 2-D simulations will not generalize to 3-D measurements.

## V. CONCLUSIONS

Tissues present a very broad range of histological structures that could interact with ultrasound when measuring the ESD. Applying imaging pulses in the 7–45 MHz frequency range with a 58% bandwidth and using 2-D echo simulations, we found that a narrow range of structures will be selected near  $ka = 1$  to contribute to the echo spectrum. Structures having sizes within a factor of 2 of each other near  $ka = 1$  contribute to the echo signal as a weighted linear sum, such that if the object distribution is approximately known, ESD measurements can be corrected for the acoustic weighting. If the range of scatterer sizes exceeds a factor of 2, only those nearest  $ka = 1$  will influence ESD measurements. Based on calibration measurements and KL-decompositional filtering of histology images, we showed that accurate estimation of cell sizes is possible, which is consistent with literature findings.<sup>10,11,16,35</sup> However, accurate estimation of cell-nucleus sizes is unlikely *in vivo* given the need for pulse frequencies near 50.

ESD measurements require operators to have some knowledge of cell sizes for the target tissues if they are to select frequencies giving  $ka \simeq 1$ . When  $ka < 1$ , there is a

tendency to overestimate ESD and, when  $ka > 1$ , the tendency is to underestimate ESD. Nevertheless, ESD measurement bias is predictable and remains fixed, suggesting that rank order is preserved in serial measurements in which scatterer sizes change. Also, ESD bias is expected to have little influence on ESD image contrast between regions in tissue of varying ESD.

## ACKNOWLEDGMENT

Research funded in this publication was supported in part by National Institute of Biomedical Imaging and Bioengineering of National Institutes of Health under award No. R37EB002641.

## APPENDIX A: FROM HISTOLOGY IMAGES TO IMPEDANCE MAPS

Each pixel in the histology image is composed of three 8-bit words indicating RGB colors. The green-channel value was negligible. We use the MATLAB function `rgbtoHSV` to convert each RGB pixel to an array of  $M \times 3$  floating point values between 0 and 1 to indicate hue  $h$ , saturation  $s$ , and value  $v$  (HSV), where  $v$  was negligible. Following the method of Mamou *et al.*,<sup>32</sup> we assigned a pixel to be “blue” (nuclear material) if  $0 \leq h < 0.75$  and “pink” (cytoplasmic proteins) if  $0.75 \leq h \leq 1$ . Then, for each pink pixel, we examined the  $s$  channel and assigned that pixel to an impedance value of 1.45 MRayl (fat) if  $0 \leq s < 0.2$ , 1.5 MRayl if  $0.2 \leq s < 0.4$ , 1.6 MRayl if  $0.4 \leq s < 0.6$ , and 1.7 MRayl if  $0.6 \leq s \leq 1$ . For each blue pixel, we also examined the  $s$  channel and assigned the pixel to an impedance value of 1.8 MRayl if  $0 \leq s < 0.4$ , 1.9 MRayl if  $0.4 \leq s < 0.6$ , and 2.0 MRayl if  $0.6 \leq s \leq 1$ . The values of impedance stated above were obtained from Ref. 40.

## APPENDIX B: IMPEDANCE CORRELATIONS AND THE STRUCTURE FUNCTION

This appendix describes the need for and the computation of the structure function,  $S(k)$ , as applied in Eqs. (7) and (8).

Generally, spatial correlations in acoustic impedance within tissues may be broadly divided into short- and long-range order, where wavelength of sound  $\lambda$  is the reference length. Short-range correlations (distances  $< 2\lambda$ ) account for the spatial extent of the average scatterer in a region. These correlations are modeled by an acoustic form factor<sup>7,9</sup> analogous to those applied in other scattering problems.<sup>41</sup>

In contrast, long-range impedance correlations (distances  $> 2\lambda$ ) describe the positional relationship among scatterers. If the scatterer density is less than one per pulse area, then echoes returning to the detector do not interfere and no speckle is formed. The echoes are distinct copies of scatterers interacting with the pulse. Now consider a medium in which the scatterer density is high enough to generate echoes that interfere at the detector surface but sparse enough to be randomly distributed. In this context, “random” means phase angles  $2kr'_j$  (for backscatter) within the summed factors  $e^{2kr'_j}$  are uniformly distributed between 0 and  $2\pi$ . Since individual echoes are uncorrelated, the echo spectrum is labeled incoherent and the backscatter coefficient is given by the

differential scattering cross section per area for one scatterer times  $N$ , the number of scatterers contributing.<sup>12</sup> If the scatterer density increases so that the phases of interfering echoes are not uniformly distributed, there will be a substantial coherent scattering component and  $\sigma_b$  will no longer be simply proportional to  $N$ .

Assume we can measure the location of each scatterer relative to a reference point on the detector,  $\mathbf{r}'$ . From this information, Han and O'Brien<sup>30</sup> calculated the structure function,

$$S(\mathbf{K}) = \frac{1}{N} \left| \sum_{j=1}^N e^{i\mathbf{K}\cdot\mathbf{r}'_j} \right|^2, \quad (\text{B1})$$

that they showed describes the phase effects of dense/partially correlated scatterer placement on the backscatter coefficient. For backscatter  $\mathbf{K} = 2\mathbf{k}$  and for random media  $S(k) \simeq 1$ . However, for partially correlated media  $S(k)$  deviates from unity at frequencies in the measurement bandwidth.<sup>30</sup>

<sup>1</sup>S. Fields and F. Dunn, "Correlation of echographic visualizability of tissue with biological composition and physiological state," *J. Acoust. Soc. Am.* **54**, 809–812 (1973).

<sup>2</sup>J. C. Bamber, "Theoretical modeling of the acoustic scattering structure of human liver," *Acoust. Lett.* **3**, 114–119 (1979).

<sup>3</sup>M. Ueda and H. Ichikawa, "Analysis of an echo signal reflected from a weakly scattering volume by a discrete model of the medium," *J. Acoust. Soc. Am.* **70**, 1768–1775 (1981).

<sup>4</sup>F. L. Lizzi, M. Greenebaum, E. J. Feleppaa, and M. Elbaum, "Theoretical framework for spectrum analysis in ultrasonic tissue characterization," *J. Acoust. Soc. Am.* **73**, 1366–1371 (1983).

<sup>5</sup>J. A. Campbell and R. C. Waag, "Ultrasonic scattering properties of three random media with implications for tissue characterization," *J. Acoust. Soc. Am.* **75**, 1879–1886 (1984).

<sup>6</sup>J. Hildebrand and D. Rugar, "Measurement of cellular elastic properties by acoustic microscopy," *J. Microscopy* **134**(3), 245–260 (1984).

<sup>7</sup>R. F. Wagner, M. F. Insana, and D. G. Brown, "Statistical properties of radio-frequency and envelope-detected signals with applications to medical ultrasound," *J. Opt. Soc. Am. A* **4**(5), 910–922 (1987).

<sup>8</sup>M. Insana, R. Wagner, D. Brown, and T. Hall, "Describing small-scale structure in random media using pulse-echo ultrasound," *J. Acoust. Soc. Am.* **87**(1), 179–192 (1990).

<sup>9</sup>M. Insana and D. Brown, "Acoustic scattering theory applied to soft biological tissues," in *Ultrasonic Scattering in Biological Tissues*, edited by K. Shung and G. Thieme (CRC Press, Boca Raton, FL, 1993), pp. 75–124.

<sup>10</sup>M. L. Oelze and W. D. O'Brien, Jr., "Method of improved scatterer size estimation and application to parametric imaging using ultrasound," *J. Acoust. Soc. Am.* **112**(6), 3053–3063 (2002).

<sup>11</sup>M. Fadhel, E. Berndt, E. Strohm, and M. Kolios, "High-frequency acoustic impedance imaging of cancer cells," *Ultrasound Med. Biol.* **41**(10), 2700–2713 (2015).

<sup>12</sup>P. Morse and K. Ingard, *Theoretical Acoustics* (Princeton University Press, Princeton, NJ, 1968), pp. 401–407.

<sup>13</sup>R. C. Waag, P. P. K. Lee, R. M. Lerner, L. P. Hunter, R. Gramiak, and E. A. Schenk, "Angle scan and frequency-swept ultrasonic scattering characterization of tissue," in *Ultrasonic Tissue Characterization II*, edited by M. Linzer (National Bureau of Standards, Washington, DC, 1979), Spec. Publ. 525, pp. 143–152.

<sup>14</sup>E. Franceschini and R. Guillermin, "Experimental assessment of four ultrasound scattering models for characterizing concentrated tissue-mimicking phantoms," *J. Acoust. Soc. Am.* **132**(6), 3735–3747 (2012).

<sup>15</sup>E. P. Nordberg and T. J. Hall, "Effective scatterer diameter estimates for broad scatterer size distributions," *Ultrason. Imaging* **37**(1), 3–21 (2015).

<sup>16</sup>H. Tadayyon, L. Sannachi, A. Sadeghi-Naini, A. Al-Mahrouki, W. T. Tran, M. C. Kolios, and G. J. Czarnota, "Quantification of ultrasonic scattering properties of *in vivo* tumor cell death in mouse models of breast cancer," *Transl. Oncol.* **8**(6), 463–473 (2015).

<sup>17</sup>P. Chaturvedi and M. Insana, "Error bounds on ultrasonic scatterer size estimates," *J. Acoust. Soc. Am.* **100**(1), 392–399 (1996).

<sup>18</sup>K. K. Shung, R. A. Sigelmann, and J. M. Reid, "Scattering of ultrasound by blood," *IEEE Trans. Biomed. Eng.* **BME-23**(6), 460–467 (1976).

<sup>19</sup>M. L. Oelze, W. D. O'Brien, Jr., J. P. Blue, and J. F. Zachary, "Differentiation and characterization of rat mammary fibroadenomas and 4T1 mouse carcinomas using quantitative ultrasound imaging," *IEEE Trans. Med. Imaging* **23**(6), 764–771 (2004).

<sup>20</sup>M. F. Insana, J. G. Wood, T. J. Hall, G. G. Cox, and L. A. Harrison, "Effects of endothelin-1 on renal microvasculature measured using quantitative ultrasound," *Ultrasound Med. Biol.* **21**, 1143–1151 (1995).

<sup>21</sup>H. Shi, T. Varghese, C. C. Mitchell, M. McCormick, R. J. Dempsey, and M. Kliewer, "*In vivo* attenuation and equivalent scatterer size parameters for atherosclerotic carotid plaque: Preliminary results," *Ultrasonics* **49**(8), 779–785 (2009).

<sup>22</sup>V. C. Anderson, "Sound scattering from a fluid sphere," *J. Acoust. Soc. Am.* **22**(4), 426–431 (1950).

<sup>23</sup>J. McNew and W. D. O'Brien, Jr., "Sound scattering from two concentric fluid spheres," *J. Acoust. Soc. Am.* **122**(5), 2968 (2007).

<sup>24</sup>V. Twersky, "Low-frequency scattering by correlated distributions of randomly oriented particles," *J. Acoust. Soc. Am.* **81**(5), 1609–1618 (1987).

<sup>25</sup>R. Lavarello and M. L. Oelze, "Quantitative ultrasound estimates from populations of scatterers with continuous size distributions," *IEEE Trans. Ultrason. Ferroelectr. Freq. Control* **58**, 744–749 (2011).

<sup>26</sup>A. Han and W. D. O'Brien, Jr., "Structure function for high-concentration biophantoms of polydisperse scatterer sizes," *IEEE Trans. Ultrason. Ferroelectr. Freq. Control* **62**, 303–318 (2015).

<sup>27</sup>C. Abbey, R. Zemp, J. Liu, K. Lindfors, and M. Insana, "Observer efficiency in discrimination tasks simulating malignant and benign breast lesions with ultrasound," *IEEE Trans. Med. Imag.* **25**, 198–209 (2006).

<sup>28</sup>The full-width-at-half-maximum (FWHM) width of a Gaussian pulse is  $2\sigma_x\sqrt{2\ln 2} = 2.355\sigma_x$ . The FWHM width of the corresponding Gaussian pulse spectrum is  $\sqrt{2\ln 2}/(\pi\sigma_x) = 0.375/\sigma_x$ . The spatial-frequency equivalent of a 10 MHz transmission frequency is  $2f_0/c = 12.99 \text{ mm}^{-1}$ . Since  $\sigma_x = 0.05 \text{ mm}$  at 10 MHz, the percent bandwidth is  $100(0.375/\sigma_x)/12.99 = 58\%$ .

<sup>29</sup>A. Gerig, J. Zagzebski, and T. Varghese, "Statistics of ultrasonic scatterer size estimation with a reference phantom," *J. Acoust. Soc. Am.* **113**(6), 3430–3437 (2003).

<sup>30</sup>A. Han and W. D. O'Brien, Jr., "Structure function estimated from histological tissue sections," *IEEE Trans. Ultrason. Ferroelectr. Freq. Control* **63**, 1296–1305 (2016).

<sup>31</sup>R. F. Wagner, S. W. Smith, J. M. Sandrik, and H. Lopez, "Statistics of speckle in ultrasound B-scans," *IEEE Trans. Sonics Ultrason.* **SU-30**, 156–163 (1983).

<sup>32</sup>J. Mamou, M. L. Oelze, W. D. O'Brien, Jr., and J. Zachary, "Extended three-dimensional impedance map methods for identifying ultrasonic scattering sites," *J. Acoust. Soc. Am.* **123**(2), 1195–1208 (2008).

<sup>33</sup>A. Pawlicki, A. Dapore, S. Sarwate, and W. D. O'Brien, Jr., "Three-dimensional impedance map analysis of rabbit liver," *J. Acoust. Soc. Am.* **130**(5), EL334–EL338 (2011).

<sup>34</sup>A. Luchies and M. L. Oelze, "Using two-dimensional impedance maps to study weak scattering in sparse random media," *J. Acoust. Soc. Am.* **139**(4), 1557–1564 (2016).

<sup>35</sup>G. Ghoshal, R. Lavarello, J. Kemmerer, R. Miller, and M. L. Oelze, "*Ex vivo* study of quantitative ultrasound parameters in fatty rabbit livers," *Ultrasound Med. Biol.* **38**(12), 2238–2248 (2012).

<sup>36</sup>R. Gonzalez and R. Woods, *Digital Image Processing* (Addison-Wesley, Boston, 1993), pp. 148–156.

<sup>37</sup>The covariance matrix is real, symmetric, positive semi-definite, and therefore eigenvalues are real and positive. For an orthonormal eigenvector matrix,  $\mathbf{V}^{-1} = \mathbf{V}^T$ , which is used in Eq. (15).

<sup>38</sup>If the object scattering function, represented by matrix  $\mathbf{f}'$ , is well represented as a normal random process, then the eigenvectors of covariance matrix  $\Sigma_f$  (columns of  $\mathbf{V}$ ) are both orthogonal and linearly independent. When  $\mathbf{f}'$  is not a normal process, the eigenvectors may be linearly dependent.

<sup>39</sup>N. Q. Nguyen, C. K. Abbey, and M. F. Insana, "Objective assessment of sonographic quality I: Task information," *IEEE Trans. Med. Imaging* **32**(4), 683–690 (2013).

<sup>40</sup>S. Goss, R. Johnston, and F. Dunn, "Compilation of empirical ultrasonic properties of mammalian tissues. II," *J. Acoust. Soc. Am.* **68**(1), 93–108 (1980).

<sup>41</sup>P. M. Morse and H. Feshbach, *Methods of Theoretical Physics* (McGraw-Hill, New York, 1953), Chap. 12.